Korean J. Chem. Eng., 37(8), 1394-1400 (2020)
DOI: 10.1007/s11814-020-0605-3

pISSN: 0256-1115
eISSN: 1975-7220

Electrochemical impedance analysis of proton exchange membrane fuel cells with various cathode configurations

Jaewoo Cho and Sehkyu Park†

Department of Chemical Engineering, Kwangwoon University, 20 Kwangwoon-ro, Nowon-gu, Seoul 01897, Korea
(*Received 26 March 2020 • Revised 2 June 2020 • Accepted 4 June 2020*)

Abstract−Various porous flow fields have been proposed and developed for the cathode configuration of proton exchange membrane fuel cells to replace conventional channel-land flow fields. This study demonstrates the physical properties of porous metallic flow field and gas diffusion layers and quantifies the respective resistances during the oxygen reduction reaction in proton exchange membrane fuel cells with four different cathode configurations using electrochemical impedance spectroscopy and a theoretical model. The contribution of the flow field and gas diffusion layer to the oxygen reduction reaction is discussed, along with the relationship between the physical properties of these structures and water transport in the proton exchange membrane fuel cell.

Keywords: Proton Exchange Membrane Fuel Cells, Porous Metallic Flow Field, Cathode Configuration, Water Management, Electrochemical Impedance Spectroscopy

INTRODUCTION

Fuel cell capable of generating electricity by electrochemical hydrogen combustion is a promising alternative to conventional combustion engines that release greenhouse gases. Among the various types of fuel cells, proton exchange membrane fuel cells (PEMFCs) have many distinctive advantages for stationary and transportation applications with zero carbon emission [1-3]. Notably, their low operating temperature (<100 °C) and high stability owing to the use of solid polymer electrolytes that serve as proton conductors and gas separators have attracted the interest of many energy researchers and manufacturers [4-6].

In PEMFCs, hydrogen and oxygen molecules are introduced at the anode and cathode, respectively. Each reactant moves along the flow field (FF) by convection and diffuses to the catalytically active sites in the catalyst layer (CL) through the gas diffusion layer (GDL). The convective flow of the reactants can be controlled based on the FF design, where the gas flow rate and distribution inside the fuel cell can be varied because the gas pressure drop and water discharge rate are greatly dependent on the FF structure [7,8]. There have been many experimental and theoretical studies on various FF structures and properties in the views of mass transport and durability in PEMFCs [9-11]. Gas diffusion occurs owing to the concentration difference between the FF and the CL (where a reactant is consumed). Gas diffusion is divided into two regimes: intermolecular diffusion in macropores and non-molecular diffusion in nano- or subnanometer pores and thin films such as the ionomer and liquid water in the CL [12-14]. GDLs with a porous structure are typically utilized to ensure effective heat and mass transfer, which depends on the void space and pore size distribution (PSD) of the GDL [15-17]. As a result, the mass transfer rate in PEMFCs is greatly affected by the structure of the FF, GDL, and CL in sequence.

To achieve stable operation at high current density (>2.0 A cm^{-2}), fast oxygen diffusion and effective water removal, especially at the cathode, are necessary. To decrease concentration losses, on one hand, many researchers have focused on novel GDL structures, validated by experimental and/or theoretical investigations. On the other hand, considerable effort has been devoted to developing a variety of flow patterns based on the channel-land flow field (CLFF) [18-21]. In general, an ideal FF must meet several requirements: i) even reactant distribution, ii) fast water elimination, and iii) good electrical contact with other components. The CLFF as a conventional FF primarily removes liquid water in the channel; however, it causes a high pressure drop due to plug flow along the channel and fails to remove liquid water accumulated on the land, thereby accelerating uneven oxygen distribution throughout the cathode. To cope with these issues, several researchers have proposed new FFs such as felt, foam, and mesh as alternatives to the CLFF [21-24]. Mench and co-workers attempted to develop a porous metallic FF (PMFF) able to fuel cell operation at high current densities (>3.0 A cm^{-2}) [21,25,26]. By designing PEMFCs with a CLFF and an open metallic element, they achieved enhanced fuel cell performance by using an open metallic FF. Based on limiting current analysis, they claimed that decreased oxygen transport resistance was achieved owing to the open metallic element that enables even distribution of water in the GDL and prevents severe water accumulation [26]. Joo et al. also developed a self-supporting microporous layer (MPL) and placed it on a metal mesh without a carbon backing at the cathode in a PEMFC [24]. They demonstrated that the carbon backing-free MPL on metal mesh alleviated the mass transport limitation at high current densities.

In this study, we introduce a three-dimensional (3D) porous metal foam as a cathode FF and examine the polarization characteristics of PEMFCs with four different cathode configurations: i) carbon

†To whom correspondence should be addressed.
E-mail: vitalspark@kw.ac.kr

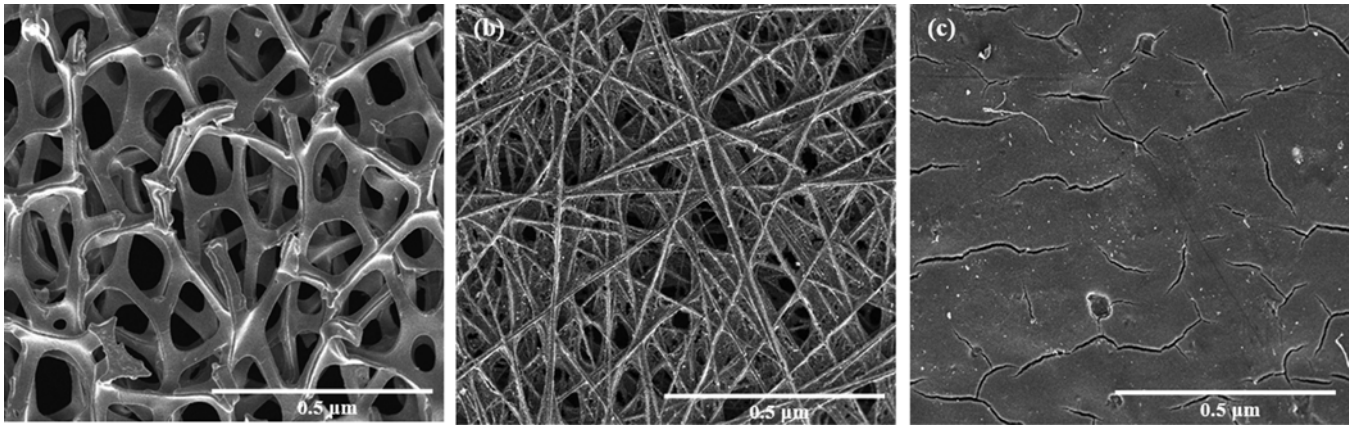

Fig. 1. SEM images of (a) PMFF, (b) CP (SGL 29AA), and (c) MPL/CP (SGL 29BC).

paper (CP) on PMFF (CP/PMFF), ii) CP on CLFF (CP/CLFF), iii) MPL-coated CP on PMFF (MPL/CP/PMFF), and iv) MPL-coated CP on CLFF (MPL/CP/CLFF). The cells are analyzed using electrochemical impedance spectroscopy (EIS), and the respective resistances during the ORR are determined by fitting the experimental data to a simplified transmission line model [27,28].

EXPERIMENTAL

1. Physical Characterization

Commercially available CP without an MPL (SGL 29AA, SGL Group Inc.) and MPL-coated CP (SGL 29BC)—5 wt% PTFE in the CP and 23 wt% PTFE in the MPL, were used as the GDLs in this study. A conventional CLFF with serpentine four flow channels (1 mm in width, depth, and spacing) and open ratio of 0.48, and a 3D PMFF (1 mm in thickness) were used as the FF. The surface morphology of the samples was observed using field-emission scanning electron microscopy (FE-SEM, Inspect F-50). The porous structures of the GDLs and PMFF were characterized by using a mercury porosimeter (Autopore V, Micromeritics Inc.). Contact angle measurements on the surface of the GDLs were carried out using a contact angle analyzer (Phoenix 300 Touch S.E.O) in accordance with the ASTM D5946 method.

2. Electrochemical Measurements

Electrochemical experiments were conducted with a commercial membrane electrode assembly (MEA, CNL Energy Inc.). The MEA was composed of NR-211 (25 μm, Dupont Inc.) and CLs on both sides of the membrane (0.1 mg_{Pt} cm^{-2} at the anode and 0.4 mg_{Pt} cm^{-2} at the cathode). Each component in the PEMFC was assembled at a constant clamping pressure (50 lb_f). Polarization experiments for the PEMFCs were performed by galvanostatic measurements using a 5 min dwell time at a constant stoichiometry of λ_{H_2}=1.5 and λ_{air}=2. The PEMFCs were operated at 65 °C with fully humidified hydrogen and air at the anode and cathode, respectively. The geometric area of the PEMFCs was 25 cm^2. EIS was carried out using a potentiostat/galvanostat (VSP, Bio-Logic Inc.) with an external current booster. The measurements were performed at 0.2 A cm^{-2} by applying a 5% AC-amplitude signal over the frequency range of 50 kHz to 50 mHz.

RESULTS AND DISCUSSION

Figs. 1(a)-(c) show the SEM images of the PMFF, CP, and MPL/CP, respectively. As observed in Fig. 1(a), the PMFF comprises a continuous array of dodecahedral cells. The numerous pentagonal and hexagonal faces in the PMFF allow fluids to penetrate, while the skeleton comprising ligaments and nodes serves as the electronic pathway. In contrast, the conventional CLFF used in this study has much smaller open ratio and contact area with air as an oxidant, probably resulting in relatively poor mass transport and thermal management in PEMFC stacks [20,22]. Therefore, the PMFF is expected to facilitate gas and water transport within the uniform and distributed pores and to improve removal of heat generated by the ORR, maintaining high electrical conductivity through the 3D skeleton structure, compared to the CLFF [23]. Figs. 1(b) and (c) display the SEM images of the CP and MPL/CP surfaces. The CP is made up of numerous carbon fibres randomly stacked with the thermoset resin, while the MPL/CP has a smooth

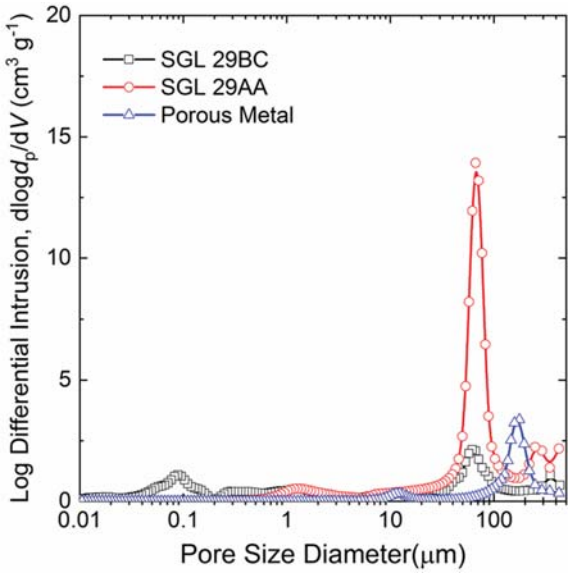

Fig. 2. PSD curves (dV/dlogd$_p$) of the GDLs and PMFF.

surface due to the microporous carbon layer applied to the CP.

Fig. 2 illustrates the pore size distribution (PSD) curves ($dV/dlogd_p$) of the PMFF, CP, and MPL/CP. The PSD of the PMFF primarily corresponds to macropores with d_p>100 μm. The PSD of the CP shows a single peak corresponding to pores with diameters of 40-100 μm, although larger pores (presumably relevant to irregular pore structure on its surface) with d_p>100 μm were observed. However, in the case of the MPL/CP, a dual-PSD was observed for the MPL at 0.08<d_p<0.2 μm and for CP between 40< d_p<100 μm. From the comparison of the PSD of the CP versus that of the MPL/CP, it is inferred that the decreased pore volume of the latter at 70 μm is attributable to the intrusion of carbon particles from the CP into the MPL during preparation of the MPL.

Oxygen diffusion is also affected by water transport in the GDL; hence, the wettability of the GDL is also a critical parameter influencing the PEMFC performance. To examine the hydrophobicity of the two different GDLs, contact angle measurements were performed. Fig. 3 shows the side-views of a water drop in contact with the surface of the GDLs. The contact angles for the CP and the MPL/CP were 120 and 150°, respectively. It is generally accepted that the contact angle of water on a surface is dependent on the surface wettability and morphology. Herein, as mentioned previously, a hydrophobic polymer is present in both the CP and MPL components of MPL/CP (SGL 29BC), while the CP (SGL 29AA) is PTFE-free. For the CP, the graphitized carbon fibres incorporated with thermoset resin in the course of carbonization at high temperature (>2,000°) may provide relatively weak hydrophobicity in the absence of PTFE, while the strong hydrophobicity of MPL/CP is associated with the microporous structure and high PTFE content in the MPL. Thus, a an MPL with the optimal PTFE content is beneficial for water management at the cathode at high current densities.

To determine the polarization characteristics of the PEMFCs with different cathode components, four different combinations of FFs and GDLs were used at the cathode: CP/PMFF, CP/CLFF, MPL/CP/PMFF, and MPL/CP/CLFF. Fig. 4(a) presents the polarization curves of CP/PMFF and CP/CLFF. As seen in Fig. 4(a), CP/PMFF was more polarizable than that of CP/CLFF in intermediate and

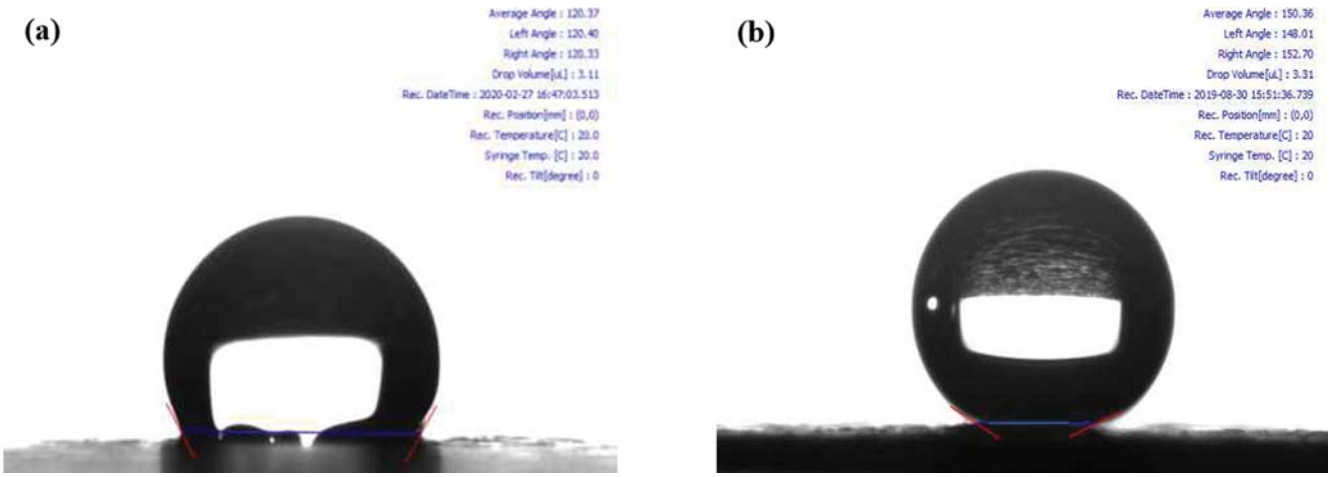

Fig. 3. Contact angle of water with (a) CP (SGL 29AA) and (b) MPL/CP (SGL 29BC).

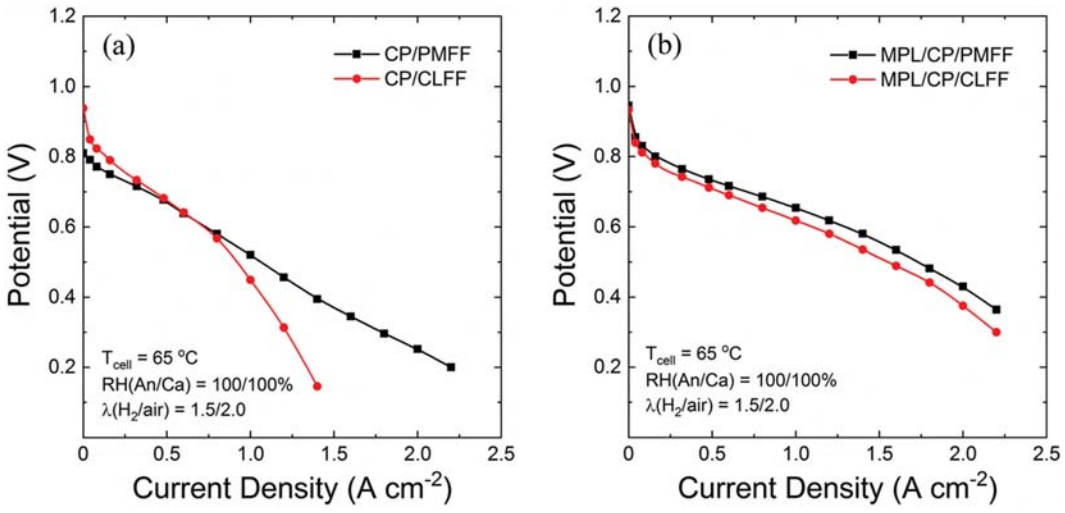

Fig. 4. Polarization curves of PEMFCs with (a) CP/PMFF and CP/CLFF and (b) MPL/CP/PMFF and MPL/CP/CLFF.

high current densities, indicating that the PMFF allows more oxygen to access the CL. However, a lower open circuit voltage was observed for CP/PMFF. This is possibly assigned to the poor contact between the CL and the CP, and/or the CP and the PMFF under the same clamping force, regardless of cathode configurations, resulting from rough PMFF surface and small contact area with the CP, compared to the CLFF that provides smooth surface and small open ratio (0.48). On the other hand, with the insertion of the MPL into the cathode, polarization of the PEMFCs was substantially higher with both the MPL/CP/PMFF and the MPL/CP/CLFF, as depicted in Fig. 4(b). Furthermore, the PMFF resulted in better PEMFC performance than the CLFF with the same MPL/CP. The experimental polarization data suggest that the MPL vastly contributes to eliminating water from the CL and the PMFF has a higher effective porosity to enable oxygen diffusion.

The EIS technique was used to distinguish the electrochemical processes at various relaxation times for the different cathode configurations. The respective polarization losses were estimated from the Nyquist plot obtained at a constant current through graphical analysis using the lumped equivalent circuit model (see Fig. 5(a)). In this model, the impedance response of total location in the CL is given as

$$Z=Z_{re}+jZ_{im} \tag{1}$$

where

$$Z_{re}=R_{H^+}+\frac{\left(\frac{1}{R_{ORR}}\right)}{\left(\frac{1}{R_{ORR}}\right)^2+(\omega\cdot C_d)^2} \tag{2}$$

$$Z_{im}=\frac{-\omega\cdot C_d}{\left(\frac{1}{R_{ORR}}\right)^2+(\omega\cdot C_d)^2} \tag{3}$$

where Z_{re} is the total real impedance in the CL, Z_{im} the total imaginary impedance in the CL, R_{H^+} the total proton resistance, R_{ORR} the total ORR resistance in the CL, ω the radial frequency, C_d the total double-layer capacitance in the CL. The details of the procedure for quantitatively determining the critical parameters using graphical analysis have been presented previously by Yi and coworkers [27,28].

Figs. 5(b)-(d) display two theoretical models for charge transfer

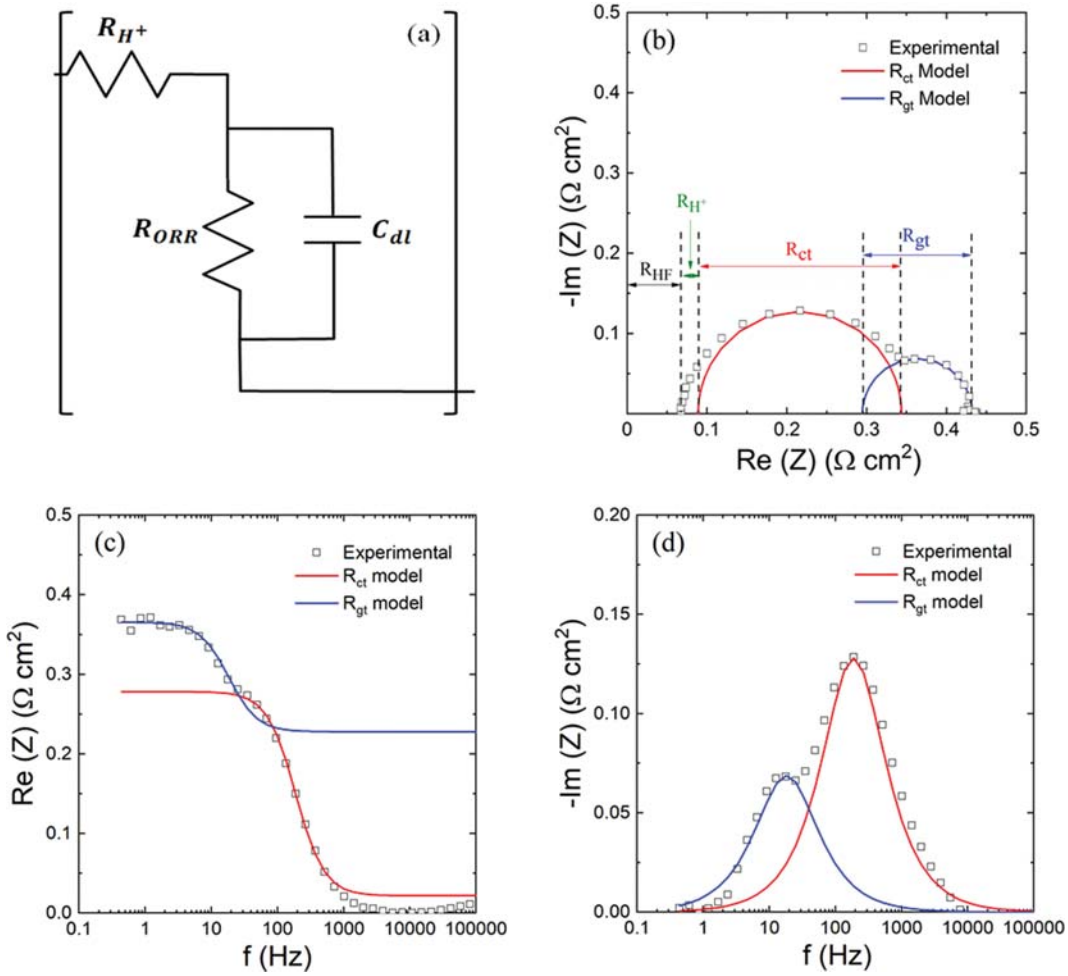

Fig. 5. (a) Lumped equivalent circuit model for the cathode; (b) Nyquist plot for the PEMFC with CP/PMFF. Graphical analysis for determining the individual resistances from the experimental EIS data; (c) Bode plots in the plane of real impedance vs. frequency, fitted to lumped circuit model; and (d) Bode plots in the plane of imaginary impedance vs. frequency, fitted to lumped circuit model.

resistance R_{ct} and gas transfer resistance R_{gt}, which were used to fit the experimental EIS data (for the CP/PMFF) in the Nyquist and Bode plots. As clearly observed in Fig. 5(b)-(d), the R_{ct} and R_{gt} models are strongly frequency-dependent. According to Kwon et al. who compared impedance between normal fuel cell condition and hydrogen pump condition, the relative magnitude of anodic impedance was significantly smaller than that of cathodic charge transfer impedance [29]. Hence, assuming that the anodic contribution is negligible compared to the cathodic processes, as shown in Fig. 5(b), the *x*-intercept observed at a high frequency in the Nyquist plot (high frequency resistance, R_{HF}) represents the ohmic resistance attributed to proton conduction across the membrane and electron transfer through the electro-conducting materials. The first arc appearing at high and intermediate frequencies represents the R_{ct} at the interface between the electrode and electrolyte during the ORR. Using the forward reaction in the Butler-Volmer equation, the kinetics expression for the ORR is as follows [27]:

$$i = i_0 A_{Pt}\left(\frac{C_{O_2}}{C^*_{O_2}}\right)\exp\left(\frac{4\alpha F}{RT}\eta_{ORR}\right) \quad (4)$$

By rearranging Eq. (4), $R_{ORR}=d\eta_{ORR}/di$ can be derived:

$$R_{ORR} = \frac{RT}{4\alpha F}\left[\frac{1}{i} - \frac{1}{i_0}\frac{di_0}{di} - \frac{1}{A_{Pt}}\frac{dA_{Pt}}{di} - \frac{1}{C_{O_2}}\frac{dC_{O_2}}{di}\right] \quad (5)$$

where i is the applied current density, i_0 is the exchange current density for the ORR when the concentration of O_2 at the reaction site is $C^*_{O_2}$, A_{Pt} is the active surface area in the CL, C_{O_2} is the average concentration of the reactant at the reaction sites, α is the transfer coefficient for the ORR, F is the Faraday constant, R is the gas constant, T is the cell temperature, and η_{ORR} is the overpotential for the ORR. R_{ORR} is mainly governed by the four terms in parentheses in Eq. (5) (i, i_0, A_{Pt}, and C_{O_2}). i_0 is primarily determined by the specific catalyst materials and electrolytes in the CL. However, the second term in parentheses in Eq. (5) can be cancelled because the same electrode materials were used in this study. The change in A_{Pt} is regarded to be insignificant during the ORR; hence, the third term can also be ignored under low and constant current density with no appreciable change in the operating conditions. Therefore, R_{ORR} is a function of the oxygen concentration at the catalyst surface, C_{O_2}, depending on the oxygen consumption rate. C_{O_2} is expected to be greatly influenced by the oxygen transfer resistance through the hydrated ionomer thin film between pressure-independent resistances [27]. The difference between the experimental and theoretical *x*-intercept at high frequencies may be interpreted as the proton transfer resistance in the CL because proton conduction along the distributed electrolyte in the reactive region takes place prior to charge transfer at the electrode/electrolyte interface [30,31]. Lastly, the second arc typically emerges at low frequencies in the presence of severe gas transfer restriction [32-34]. Hence, the magnitude of this arc is strongly affected by the oxygen concentration gradient through the gas-phase void and thin ionomer film. Consequently, using this methodology, four individual resistances, R_{HF}, R_{H^+}, R_{ct}, and R_{gt} during the ORR can be quantitatively distinguished, thereby providing useful information on how the cathode configuration with different GDLs and FFs influences the polarization characteristics of the PEMFC.

To distinguish the respective resistances, AC impedance measurements were performed at a constant current of 0.2 A cm^{-2}, where it is thought that R_{gt} at the cathode is much smaller than R_{ct} at the interface between the electrode and the electrolyte. Typically, when oxygen diffusion is the limiting step in the PEMFC, the second arc becomes substantially larger, thereby offsetting the effects of other processes [27,28]. Furthermore, the aforementioned variation of i_0 and A_{Pt} may be more severe at high current densities where mass transport limitation appears, which may plausibly lead to incorrect estimation of the individual resistances.

Fig. 6(a) shows the Nyquist plots from the AC impedance data for the PEMFCs with the CP on different FFs. EIS measurements were conducted at 65 °C and 0.2 A cm^{-2}. The impedance spectra of the PEMFCs with different cathode configurations were evidently different, although the current density was the same, which led to insignificant voltage loss during the EIS measurement. The individual resistances obtained from the graphical analysis are summarized in Fig. 6(b). A marginally higher R_{HF} was found for the

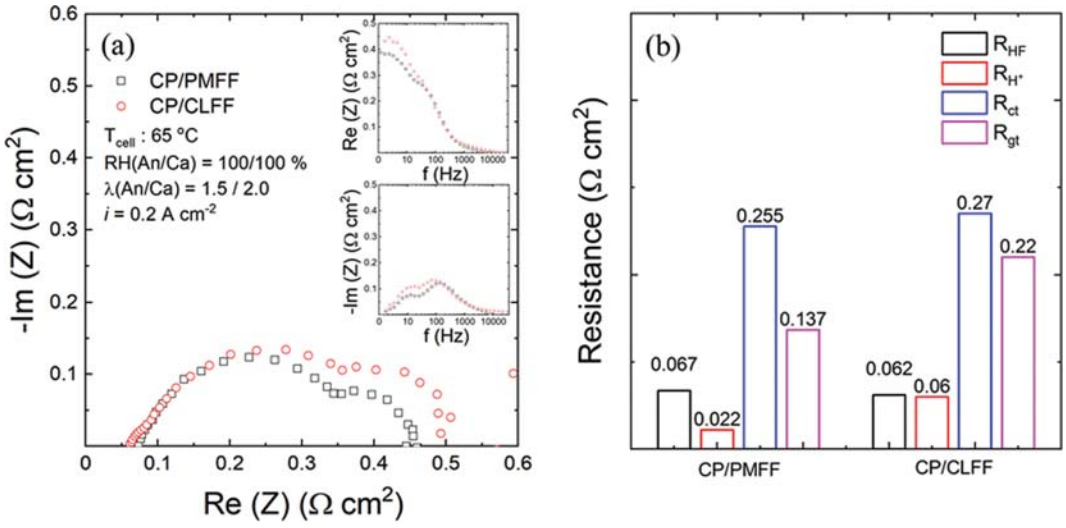

Fig. 6. (a) Nyquist plots of PEMFCs with CP/PMFF and CP/CLFF and (b) comparison of respective resistances during the ORR.

CP/PMFF, plausibly associated with the relatively high contact resistance between the CP and the PMFF (possibly due to the smaller contact area) and/or between the PMFF and the end plate, although the PEMFC was under the same compression. To ensure that R_{HF} is mainly associated with contact resistance, the electrical resistivity of two FFs was estimated and the PMFF was smaller electrical resistivity by about one order of magnitude than that of the CLFF. This indicates electrical resistivity of FFs in this study did not remarkably influence R_{HF}. It is postulated that the polarization characteristics, where a relatively low open circuit voltage was observed for the CP/PMFF (Fig. 4(a)), can be attributed to the aforementioned contact resistance. However, for the CP/PMFF, R_{H^+} was approximately 2.7-fold smaller than that for the CP/CLFF, indicating that proton transfer in the CL for the CP/PMFF is better than that for the CP/CLFF, presumably owing to the more uniform water distribution throughout the CL. Nonetheless, R_{HF} and R_{H^+} have a minor effect on the total polarization because sufficient hydration of both the membrane and the ionomer was achieved with the fully humidified fuel and oxidant. On the other hand, as clearly observed from the first and second arcs in Fig. 6(a), the main polarization losses arise from the charge and gas transfer processes. By comparing R_{ct} with R_{gt} from graphical analysis of the EIS data, the difference in the R_{gt} of the CP/PMFF and CP/CLFF is more significant than the difference between the R_{ct} values for these two configurations. The results suggest greater suppression of oxygen transfer through the CP/CLFF due to greater water saturation at the cathode compartment. Thus, the CP/PMFF allows water to drain rapidly out of the CL, thereby reducing the oxygen diffusion resistance. In addition, the slight difference in R_{ct} for the CP/PMFF and CP/CLFF is believed to originate from the significantly different oxygen transfer resistance, which in turn determines the oxygen concentration at the catalyst surface.

Fig. 7(a) depicts the Nyquist plot of the MPL/CP/PMFF and the MPL/CP/CLFF, and the individual resistances for these configurations are presented in Fig. 7(b). The similar R_{HF} values suggest that the MPL applied on the CP improves the electrical contact at the interface between the CL and the GDL. Unlike the cathode with the PMFF, the values of R_{H^+} for the PEMFC with CLFF are strongly dependent on the GDL configuration. This may indicate that the MPL contributes to a relatively high-water concentration at the CL/MPL interface owing to the high capillary pressure caused by the microporous structure and high hydrophobicity [18,19, 24,35]. The R_{ct} for MPL/CP/PMFF is smaller than that for MPL/CP/CLFF, whereas the R_{gt} for both FF types with MPL/CP was similar, in contrast to the R_{gt} for the single-layer GDL on the different FFs (Fig. 6(a)-(b)). It is considered that gas-phase oxygen diffusion in non-reactive regions such as the FF and GDL is not highly detrimental because of the fast water removal from the CL to the FF in the presence of the MPL (confirmed by the nearly identical values of R_{H^+}). However, the oxygen diffusion in the CL is believed to be influenced by the FF. From Eq. (5), the lower R_{ct} for the PEMFC with the PMFF may be ascribed to the improved interfacial oxygen kinetics, depending on the oxygen concentration on the catalyst surface. Specifically, a high-water removal rate owing to the PMFF with uniformly distributed macropores is expected to lead to decreased local oxygen resistance through the hydrated ionomer film and diffusion in the Knudsen regime. In addition, the superior fuel cell performance achieved with the MPL/CP/PMFF can be interpreted in terms of the non-cylindrical pore structure and wettability gradient. As shown in Figs. 1 and 2, numerous thickened capillaries from the CL to the FF with decreasing hydrophobicity along the pore could be constructed using the MPL/CP/PMFF configuration at the cathode, which in turn increased the rate of water discharge to the FF, thereby enabling higher oxygen flux to the active sites.

CONCLUSION

PEMFCs with different GDLs and FFs were examined by ex situ characterization, including SEM, mercury porosimetry and contact angle analysis, and in situ electrochemical measurements using the polarization technique and EIS. A simplified transmission line model was also introduced to determine the respective resistances during the ORR. The experimental and theoretical results in this

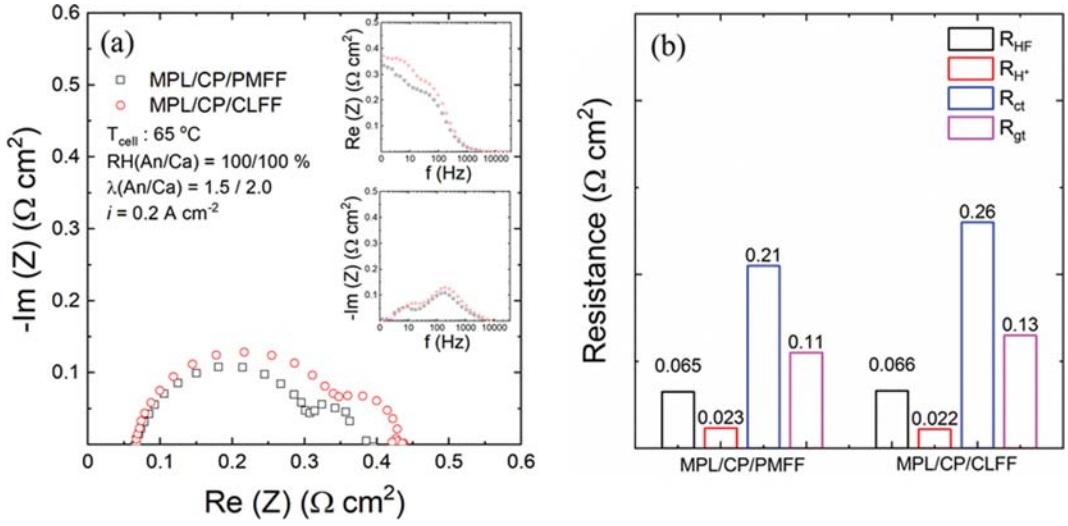

Fig. 7. (a) Nyquist plots of PEMFCs with MPL/CP/PMFF and MPL/CP/CLFF and (b) comparison of respective resistances during the ORR.

study indicate that i) the PMFF considerably increases the water removal rate in the absence of the MPL at the cathode, thus improving oxygen transport in the GDL, ii) the MPL substantially contributes to water management in the GDL, regardless of the FF type; and iii) the MPL/CP/PMFF configuration reduces water accumulation in both the CL and the GDL, thereby enhancing the kinetics of the oxygen reduction reaction.

ACKNOWLEDGEMENTS

Financial support from a National Research Foundation of Korea (NRF) grant, funded by the Korean Government (MSIT) (nos. 2019R1A2C1085095 and 2019M3E6A1064708) is gratefully acknowledged. JC and SP thank Jung S. Yi for the EIS analysis. This work was conducted during the sabbatical year of Kwangwoon University in 2020.

REFERENCES

1. S. G. Chalk and J. K. Miller, *J. Power Sources*, **159**, 73 (2006).
2. S. Park, Y. Shao, J. Liu and Y. Wang, *Energy Environ. Sci.*, **5**, 9931 (2012).
3. S. J. Peighambardoust, S. Rowshanzamir and M. Amjadi, *Int. J. Hydrogen Energy*, **35**, 9349 (2010).
4. R. K. Ahluwalia and X. J. Wang, *J. Power Sources*, **177**, 167 (2008).
5. A. Chandan, M. Hattenberger, A. El-Kharouf, S. Du, A. Dhir, V. Self, B. G. Pollet, A. Ingram and W. Bujalski, *J. Power Sources*, **231**, 264 (2013).
6. S. G. Kandlikar and Z. Lu, *Appl. Therm. Eng.*, **29**, 1276 (2009).
7. A. Aiyejina and M. K. S. Sastry, *J. Fuel Cell Sci. Tech.*, **9**, 1 (2012).
8. K. Cho and M. M. Mench, *Int. J. Hydrogen Energy*, **35**, 12329 (2010).
9. W. Li, Q. Zhang, C. Wang, X. Yan, S. Shen, G. Xia, F. Zhu and J. Zhang, *Appl. Energy*, **195**, 278 (2017).
10. A. P. Masno, F. F. Marzo, J. Barranco, X. Garikano and M. G. Mujika, *Int. J. Hydrogen Energy*, **37**, 15256 (2012).
11. N. F. Asri, T. Husaini, A. B. Sulong, E. H. Majlan and W. R. W. Daud, *Int. J. Hydrogen Energy*, **42**, 9135 (2017).
12. D. R. Baker, D. A. Caulk, K. C. Neyerlin and M. W. Murphy, *J. Electrochem. Soc.*, **156**, B991 (2009).
13. N. Nonoyama, Okazaki, A. Z. Weber, Y. Ikogi and T. Yoshida, *J. Electrochem. Soc.*, **158**, B416 (2011).
14. T. Mashio, A. Ohma, S. Yamamoto and K. Shinohara, *ECS Trans.*, **11**, 529 (2007).
15. S. Park, J. Lee and B. N. Popov, *Int. J. Hydrogen Energy*, **37**, 5850 (2012).
16. J. St-Pierre, *Fuel Cells*, **2**, 263 (2011).
17. L. Cindrella, A. M. Kannan, J. F. Lin, K. Saminath, Y. Ho, C. W. Lin and J. Wertz, *J. Power Sources*, **194**, 146 (2009).
18. S. Park, J. Lee and B. N. Popov, *J. Power Sources*, **163**, 357 (2006).
19. S. Park and B. N. Popov, *Fuel*, **90**, 436 (2011).
20. M. P. Manahan, M. C. Hatzell, E. C. Kumbur and M. M. Mench, *J. Power Sources*, **196**, 5573 (2011).
21. M. P. Manahan and M. M. Mench, *J. Electrochem. Soc.*, **159**(7), F322 (2012).
22. A. K. Srouji, L. J. Zheng, R. Dross, A. Turhan and M. M. Mench, *J. Power Sources*, **218**, 341 (2012).
23. Y. Sim, J. Kwak, S. Kim, Y. Jo, S. Kim, S. Kim, J. Kim, C. Lee, J. Jo and S. Kwon, *J. Mater. Chem. A*, **6**, 1504 (2018).
24. D. Joo, S. M. Jin, J. H. Jang and S. Park, *Fuel Cells*, **18**, 57 (2018).
25. A. K. Srouji, L. J. Zheng, R. Dross, A. Turhan and M. M. Mench, *J. Power Sources*, **239**, 433 (2013).
26. A. K. Srouji, L. J. Zheng, R. Dross, D. Aaron and M. M. Mench, *J. Power Sources*, **364**, 92 (2017).
27. J. Kim, J. S. Yi and T. Song, *J. Power Sources*, **220**, 54 (2012).
28. J. S. Yi and T. Song, *J. Electrochem. Soc.*, **160**(2), F141 (2013).
29. K. Kwon, J. O. Park, D. Y. Yoo and J. S. Yi, *Electrochim. Acta*, **54**, 6570 (2009).
30. R. Makharia, M. F. Mathias and D. R. Baker, *J. Electrochem. Soc.*, **152**, A970 (2005).
31. D. Malevich, B. R. Jayasankar, E. Halliop, J. G. Pharoah, B. A. Peppley and K. Karan, *J. Electrochem. Soc.*, **159**(12), F888 (2012).
32. T. E. Springer, T. A. Zawodzinski, M. S. Wilson and S. Gottesfeld, *J. Electrochem. Soc.*, **143**, 587 (1996).
33. Q. Guo and R. E. White, *J. Electrochem. Soc.*, **151**, E133 (2004).
34. I. A. Schneider, S. A. Freunberger, D. Kramer, A. Wokaun and G. G. Scherer, *J. Electrochem. Soc.*, **154**, B383 (2007).
35. F. C. Cetinbas, R. K. Ahluwalia, A. D. Shum and I. V. Zenyuk, *J. Electrochem. Soc.*, **166**(7), F3001 (2019).